

Cyclic microbridge testing of graphene oxide membrane

Quan Wu ^a, Zhaohe Dai ^c, Yanjing Su ^{a,*}, Alex A. Volinsky ^b, Luqi Liu ^c, Zhang Zhong ^c

^a Corrosion and Protection Center, Key Laboratory for Environmental Fracture (MOE), University of Science and Technology Beijing, Beijing 100083, China

^b Department of Mechanical Engineering, University of South Florida, Tampa, FL 33620, USA

^c National Center for Nanoscience and Technology China, Beijing 100190, China



ARTICLE INFO

Article history:

Received 28 October 2016

Received in revised form

29 January 2017

Accepted 9 February 2017

Available online 17 February 2017

ABSTRACT

Theoretical formula to determine flexible membrane deformation of microbridge test was derived based on the assumption that the membrane deformation is dominated by stretching, opposite to bending. Microbridge samples were fabricated from 0.17 μm thick free-standing graphene oxide membrane placed on patterned silicon substrates and tested with a nanoindentation system. The effective Young's modulus was determined from the microbridge test during both loading and unloading. Combining the flexible membrane theoretical formula with deformable tension-shear model, a multiscale model was proposed to determine the shear modulus of graphene oxide membrane. The effect of temperature on Young's modulus in different loading sequence was investigated. Polarized Raman spectroscopy and X-ray diffraction were utilized to characterize the self-stiffening behavior of graphene oxide membranes.

Published by Elsevier Ltd.

1. Introduction

Graphene oxide (GO) sheet is considered to be one of the most important graphene derivatives, which contains various oxygen groups (including epoxy, hydroxyl, carboxyl, carbonyl and so on) [1] attached to the graphene basal plane and the edge. The presence of these hydrophilic functional groups allows individual GO sheets to easily assemble into multilayer membranes through simple filtration or liquid/air interface self-assembly technique [2,3]. Recently, GO membranes have captured more attention due to their potential applications as gas separation membranes, biosensors, supercapacitors and humidity sensors [4–7]. Thus, accurate determination of the GO membrane mechanical properties is quite important.

Chen. et al. [2] demonstrated that the GO film deformation process has self-reinforcement and elastic deformation steps. Some interesting deformation behavior was reported using the GO membrane cyclic tensile test. Dikin. et al. [3] systematically studied and characterized free-standing GO films. The elastic modulus increased by 20% after five cyclic loading experiments, which was called the self-reinforcing behavior. On the other hand, Park. et al. [8] investigated mechanical properties of the modified GO films with divalent ions. In their study, cyclic loading experiments

showed that only modified GO membranes instead of pure GO membranes exhibited elastic self-reinforcing behavior, which is quite different from the Dikin's results [3]. What's more, Hu et al. assembled GO into hydrogels in ethylenediamine aqueous solution to produce ultralight graphene aerogel by microwave irradiation [9]. The elastic modulus of ultralight graphene aerogel apparently decreased during compression cycle experiments conducted five times. According to the results obtained so far, GO's Young's modulus variation in cyclic loading experiments is still a debate. Moreover, the reported tensile modulus [10,11] of the micron-scale GO membranes had a relatively wide range of 3.4–42 GPa, which is much higher than other carbon materials, such as bucky paper and flexible graphite. This variance is not only rooted from wrinkles [12], water content [13,14], interlayer interactions [11,15] and so on, but also strongly depends on temperature [16,17]. Thermogravimetric analysis [18] of GO membranes under ambient atmosphere shows that there are three stages in the process of mass loss, including removal of adsorbed water at 100 °C, decomposition of oxygen-containing functional groups at 200 °C, and combustion of grapheme at 550 °C. Chen et al. found that the Young's modulus of GO paper decreased when the temperature rose from 100 °C to 220 °C [16]. However, the change of Young's modulus below 200 °C in cyclic loading tests has not been studied yet.

Nowadays, a variety of novel mechanical characterization methods have been proposed. They can be classified into two categories: the whole and the representative volume elements of the nanocomposite characterization methods. Based on the whole

* Corresponding author.

E-mail addresses: yjsu@ustb.edu.cn (Y. Su), volinsky@usf.edu (A.A. Volinsky).

nanocomposite (WN) characterization methods, the nanocomposite is regarded as an integrated entity. The nominal characterization parameters can be derived from combining mechanical response with mechanical deformation models, while deformation of the inner structures is not well understood. According to the representative volume element of the nanocomposite (RVEN) characterization methods, the nanocomposite is constructed by repeatedly stacking representative volume element cells, which vary for different materials. Deformation of the inner structures is clear, while characteristic dimensions of the RVEN are hard to determine. Hence, combining the two methods seems to be a better choice.

Among the WN characterization methods, micro/nanobridge testing is one of the most important experimental measurements. Micro/nanobridge tests involve clamping nanobeams/nanoribbons over trenches on a substrate by self-adhesion or electron-beam-induced deposition processes between the nanobeams/nanoribbons and the substrate. Extracting mechanical properties of the nanobeams/nanoribbons from the experimental force-deflection curves under a single-point or lateral loads can be achieved using atomic force microscopy (AFM) or nanoindentation. Deformation of the nanobeams/nanoribbons could be bending or stretching, or both. In the Zhang's model [19] of bridge large deflection, which is based on the classical laminated beam theory, deformation of the bridge included flexural deformation along the microbridge thickness direction and tensile deformation along the microbridge length direction. Since the microbridge length or deflection is much larger than the thickness, tensile deformation along the microbridge length direction may be predominant. A membrane deflection model was proposed by Espinosa [20] and Herbert [21], which assumed that the effects of bending moments could be ignored, meaning that the deformation of the film is responsible for stretching rather than bending and the supporting substrate is infinitely stiff. This model was applied to determine mechanical properties of suspended metallic films [21] and graphene ribbon [22]. The effective Young's modulus of the multilayer GO can be obtained by fitting the experimental load-deflection curves with the deformation models mentioned above, while ignoring the interaction of each GO sheet in the layer-by-layer hierarchical structures.

According to the RVEN characterization methods, there are several existing theoretical models to treat the mechanics of composites with hierarchical structures. To model tensile behavior of nacre, a shear lag model was developed by Kotha et al. [23], which accounted for interactions between the overlapping platelets. Ji and Gao [24] proposed a tension-shear (TS) chain model to study mechanical properties of biological materials with hierarchical microstructure. In the tension-shear chain model the mineral bones are considered as rigid bars or platelets, so the shear stress at the interface between the mineral and the protein is uniform. Liu et al. [25] proposed deformable tension-shear model to predict the mechanics of graphene-based paper materials under tensile loading. In the tension-shear model, the elastic deformation of the graphene sheets, the interlayer and the intralayer crosslinks are fully considered.

In this study, the 0.17 μm thick GO microbridge samples were fabricated using semiconductor technology and focused ion beam micro-nano processing technology. Combination of the WN and RVEN methods was adopted to characterize the GO membrane deformation. Based on the most reliable WN model, the cycle loading experiment is theoretically analyzed to explain the effective Young's modulus change of the GO membrane. The shear modulus of the GO membrane is determined by obtaining the effective Young's modulus using the RVEN model. The impact of temperature on effective Young's modulus in different loading

sequences was investigated. Combining polarized Raman spectroscopy and X-ray diffraction, hierarchical microstructure evolution of assembled graphene was obtained to analyze the self-stiffening behavior of graphene oxide membranes.

2. Experimental

GO microbridge specimens were fabricated on the 100 mm diameter (100) Si wafers with both sides polished. Fig. 1 (a)-(f) show schematics of the fabrication process. A layer of Si₃N₄ was first deposited on both sides of the wafer. Dry etching was used to create windows in the bottom side of the Si₃N₄ layer to expose Si underneath. After that, the wafer was immersed in KOH solution (500 g/ml) to etch Si from the bottom side of the window. After Si was etched through, wafers were placed into the HF solution to sweep away Si₃N₄. GO was prepared from purified natural graphite (obtained from Qingdao Yingshida Graphite Co., Ltd., with a particle size of 20 μm) by the modified Hummers method [34]. The GO paper was made by filtration of the resulting colloid (2 mL) through a cellulose membrane filter (47 mm in diameter, 0.22 μm pore size), followed by air drying and peeling from the filter. The free-standing GO film can be easily transferred to the as-prepared Si substrate in deionized water. After the vacuum drying process (0.05 MPa, 333 K, 12 h), microbridges were fabricated by removing material from the parent GO paper on the Si substrate using focused ion beam (FIB) integrated within scanning electron microscope (SEM). A relatively small FIB current of 1 nA was used to avoid ion beam implantation and damage of the GO samples during microbridge fabrication. The microbridge mechanical testing was conducted using Nano-indenter II equipped with a wedge indenter tip. The wedge indenter was made of diamond and had a width of 20 μm, which is wider than the sample width, so that the one-dimensional analysis holds (see Fig. 2).

3. Theoretical analysis

According to the classical laminated beam theory [26], the governing equation for the microbridge deformation is expressed by

$$D \frac{\partial^4 w}{\partial x^4} - N_x \frac{\partial^2 w}{\partial x^2} = q \quad (1)$$

where w denotes the deflection of any point on the microbridge, D denotes the flexural rigidity, N_x denotes the force per unit width in the middle plane of the film along the length direction and q denotes distributed applied lateral load per unit width. Expression for N_x is of the form

$$N_x = A \left[\frac{\partial u}{\partial x} + \frac{1}{2} \left(\frac{\partial w}{\partial x} \right)^2 \right] + N_r \quad (2)$$

where u denotes the displacement of the neutral bending plane along the x -axis. The residual force per unit width is given by $N_r = \sigma_r t$ with t being the film thickness and σ_r being the residual stress per unit width, and the tensile rigidity is expressed by $A = Y t$ with Y being the elastic modulus of the microbridge.

For flexible membrane [26], bending deformation of the bridge beam induced by the lateral load is neglected and hence the flexural rigidity D is approximately equal to zero. Thus, the governing equation for the microbridge can be reduced to

$$-N_x \frac{\partial^2 w}{\partial x^2} = q \quad (3)$$

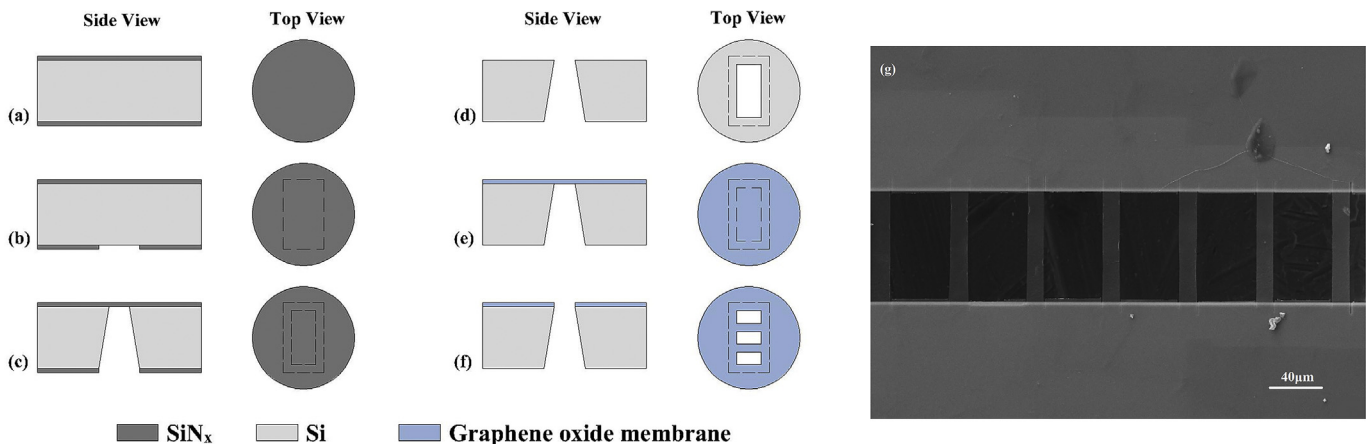


Fig. 1. (a)–(f) Fabrication flow of the GO membrane microbridge samples; (g) SEM micrograph of the bridge samples array. (A colour version of this figure can be viewed online.)

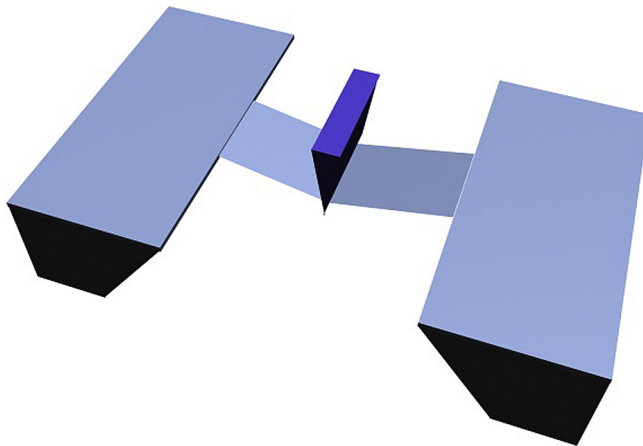


Fig. 2. Schematics of the microbridge test. (A colour version of this figure can be viewed online.)

The solution is symmetric about $x = 0$ and only the solution for $-L/2 \leq x \leq 0$ is given here for simplicity:

$$w = \frac{Q}{2N_x} \left(x + \frac{L}{2} \right) + w_0 \quad (4)$$

where w_0 denotes a deflection along the z-axis at the bridge ends and Q denotes a lateral load per unit width applied at the bridge center.

The deflection of the microbridge at the center, $x = 0$, where the lateral load is applied, is expressed by

$$w_c = \frac{QL}{4N_x} + w_0 \quad (5)$$

At the end of the microbridge, the slope of the deflection is calculated by differentiating Equation (4) with respect to x and is expressed by

$$\frac{\partial w}{\partial x} = \frac{Q}{2N_x} \quad (6)$$

Then, substituting Equations (5)–(6) into Equation (2) and integrating Equation (2) over x once, the load-deflection relationship can be rewritten as

$$Q = \frac{8tY}{L^3}(w_c - w_0)^3 + \frac{4t\sigma_r}{L}(w_c - w_0) - \frac{8tu_0}{L^2}(w_c - w_0) \quad (7)$$

where u_0 denotes a displacement along the x-axis at the bridge ends.

Since the substrate is rigid, the load-deflection relationship can be written as

$$Q = \frac{8tY}{L^3}w_c + \frac{4t\sigma_r}{L}w_c \quad (8)$$

In brief, the effective Young's modulus and the residual stress are determined from fitting the experimental load-deflection curves using Equation (8) with the least square technique to minimize the following positive function

$$S = \sum_{i=1}^n \left[Q_i^e(w_i) - Q_i^t(w_i, Y, \sigma_r) \right]^2 \quad (9)$$

Here, n denotes the number of data points, $Q_i^e(w_i)$ and $Q_i^t(w_i, Y, \sigma_r)$ denote experimentally observed and theoretically predicted deflections, respectively.

According to the deformable tension-shear (DTS) model, the representative volume element of the GO membrane is illustrated in Fig. 3. The geometry of the representative volume element is determined by the graphene oxide sheet thickness h , the sheet size l , and the interlayer distance h_0 . In this continuum model, tensile deformation of the graphene oxide sheet and the shear deformation between the out-of-plane adjacent graphene oxide layers are considered, while the tensile deformation at the edges of the in-plane adjacent graphene sheets is neglected for simplicity. Hence, the mechanical resistance of the representative volume element is equal to the tensile load F acting on the graphene oxide sheet and the interlayer shear load τ between the adjacent graphene oxide layers, when a tensile force is applied to the overall structure. In a linearly elastic approximation, the effective Young's modulus of the overall structure is determined as [25].

$$Y_{eff} = \frac{Eh}{2(h_0 + h)} \frac{1}{\frac{1+\cosh(l/l_0)}{\sinh(l/l_0)}(l/l_0)} \quad (10)$$

where E denotes the Young's modulus of the graphene oxide sheet, $l_0 = \sqrt{Eh/4G}$ denotes a typical length scale for load transfer between the out-of-plane adjacent graphene oxide sheets and G denotes the shear modulus of graphene oxide membrane. When

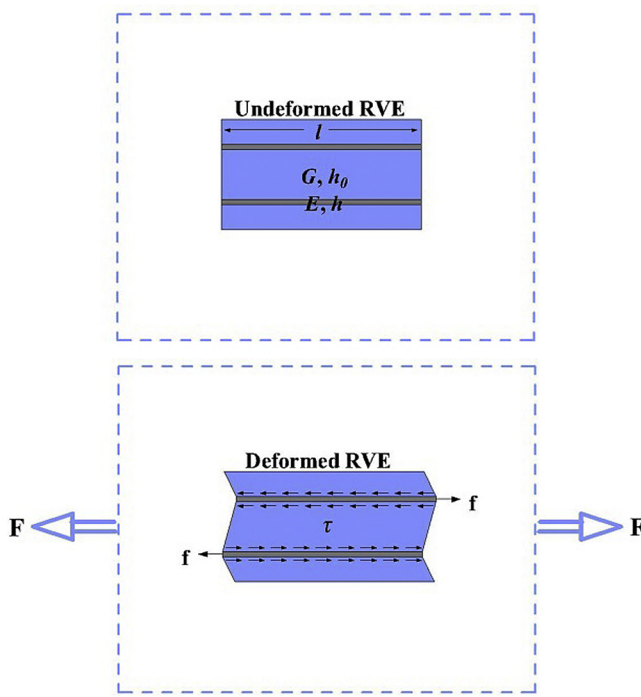


Fig. 3. An illustration of the undeformed and deformed RVE models. (A colour version of this figure can be viewed online.)

the size of the graphene oxide exceeds $3l_0$, the DTS model instead of the widely used tension-shear TS chain model is able to predict the overall mechanical properties of graphene-based papers [25,27,28].

4. Results and discussion

Fig. 4 shows typical load versus vertical displacement curves of the microbridge's center. It is found that the difference between the first loading curve and the subsequent loading-unloading curves is significant. The observed displacement hysteresis in the first cycle in regards to the subsequent cycles can be explained by the self-reinforcing behavior.

Self-reinforcing behavior is well known for polymer materials in which macromolecular movements (e.g. straightening and reorientation) would improve the alignment as well as original stiffness of curved and unaligned polymer chains at large strain levels [29]. Similarly, our GO microbridge samples should also feature highly curved and partially aligned microstructures since suspended individual GO sheets are unavoidably corrugated due to their atomic thickness and irregular distribution of oxygen-rich groups on the surface as well as thermal fluctuations [30,31]. Herein, we characterized microstructure evolution of the GO films after dynamic tension process via widely used Raman spectra technique and X-ray diffraction (XRD) patterns, as shown in **Fig. 5(a)**. For this purpose, 6 μm thick GO films were prepared (more reliable for microstructure characterization) and characterized before and after dynamic tension under 1 Hz, 0.1% strain, which is close to the strain level our microbridge samples were subjected to during indentations. In efforts to clarify the underlying structural evolution of the samples during loading, polarized Raman spectra were recorded by using an incident laser beam with the length direction at 0° and 90° with respect to the incident polarization axis of the dynamically stressed and unstressed GO films, as shown in **Fig. 5(a)**. Polarized Raman spectra were collected in the back scattering geometry using the Renishaw Raman spectrometer equipped with the 514.5 nm line of an Ar laser. Motorized x-y stage was used to vary the film angle with respect to the vector of linearly polarized excitation. The laser power was kept below 1 mW on the sample to avoid laser-induced

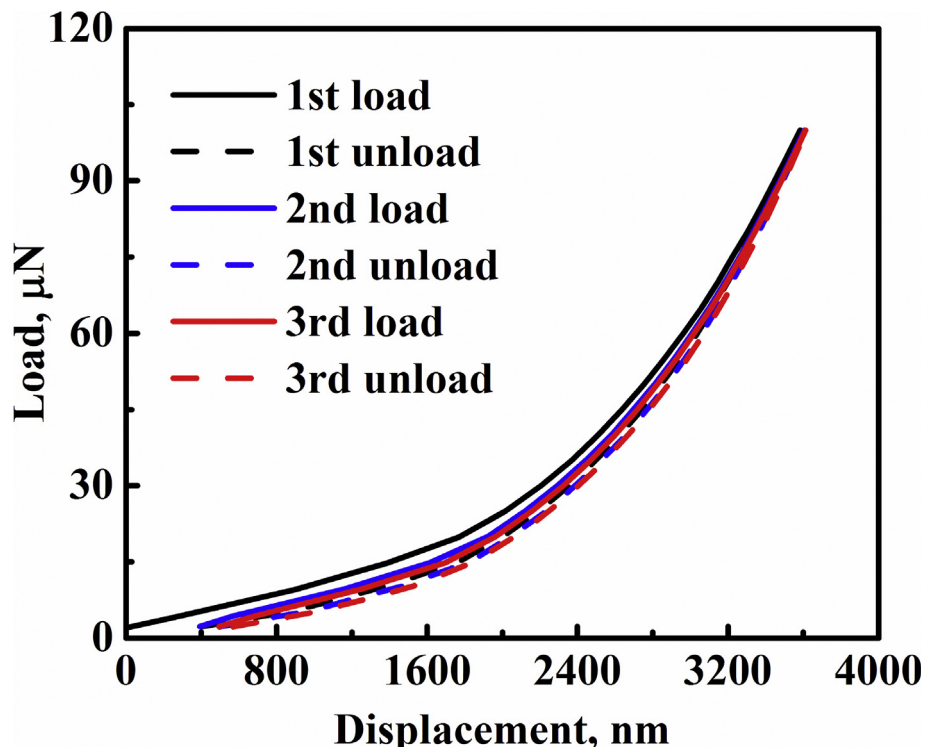


Fig. 4. Typical load versus vertical displacement curves of the microbridge. (A colour version of this figure can be viewed online.)

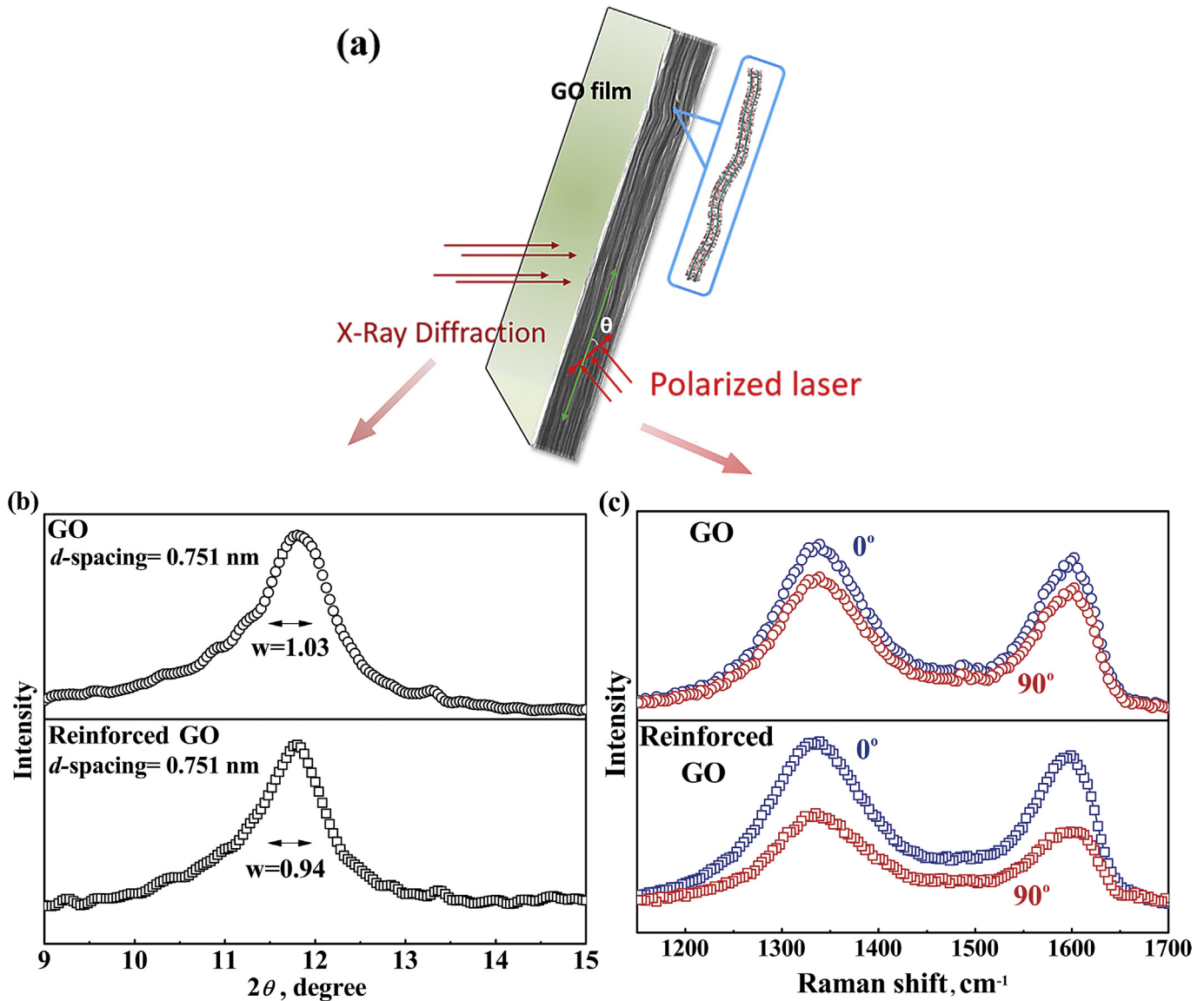


Fig. 5. (a) Schematic of the GO films geometry for XRD and Raman spectra measurements, (b) XRD patterns of GO films before and after dynamic tension, (c) typical polarized Raman spectra of the samples before and after dynamic tension. (A colour version of this figure can be viewed online.)

local heating of the sample. The incident light was first polarized along the length direction. The focused laser spot was approximately 1 μm in diameter, and the spectral resolution was ~1 cm⁻¹. In Fig. 5(c), for both stressed and unstressed samples, the peak intensities of the D band (at ~1330 cm⁻¹) and G band (at ~1600 cm⁻¹) decreased when the length axis was inclined to 90° with respect to the polarization axis, an indicator of anisotropy [30]. Moreover, the reduction of Raman peak intensity for dynamically stressed films is more notable than for unstressed samples, indicating improved anisotropy or orientation degree of the graphene sheet along the loading (length) direction. Specifically, the Raman G band intensity ratio between 0° and 90° changes from 1.2 for original samples to 2.2 for dynamically stressed films based on 20 measured spectra, implying the improvement on alignments of the graphene sheet along the loading (length) direction after dynamic stressing. XRD measurements of the film samples were performed at room temperature using specular reflection mode (Cu KR radiation $\lambda = 0.154$ nm, X'Pert PRO, PANalytical, Holland). Data were collected between 3° and 20° at 0.02°/s scan rate. XRD results in

Fig. 5(b) also reveal that dynamic stressing of the GO films does not change the interlayer distance, but the half-width at half-maximum shows a slight decrease after dynamic testing. This also indicates slightly improved orientation of the GO sheets, since generally sharper peaks in XRD patterns indicate better microstructure alignment of the graphene sheets.

Fig. 6 illustrates a comparison between the experimental load-deflection data and the theoretical predictions. The values of the effective Young's modulus and the residual stress in each cyclic loading experiment are evaluated by fitting the experimental data of 22 samples with Eq. (8).

The evaluated Young's modulus of each cyclic loading and unloading process is fitted by Eq. (8), and is plotted against the bridge length in Fig. 7. It is seen that the effective Young's modulus is statistically independent of the bridge length. For the small sample data size (less than 30 samples), the confidence intervals and the range of reliable data are determined by $\bar{x} \pm s t_{0.005}/\sqrt{n}$ and $\bar{x} \pm s t_{0.005}$, respectively, where \bar{x} denotes the average effective Young's modulus, s denotes standard deviation, $t_{0.005}$ denotes the

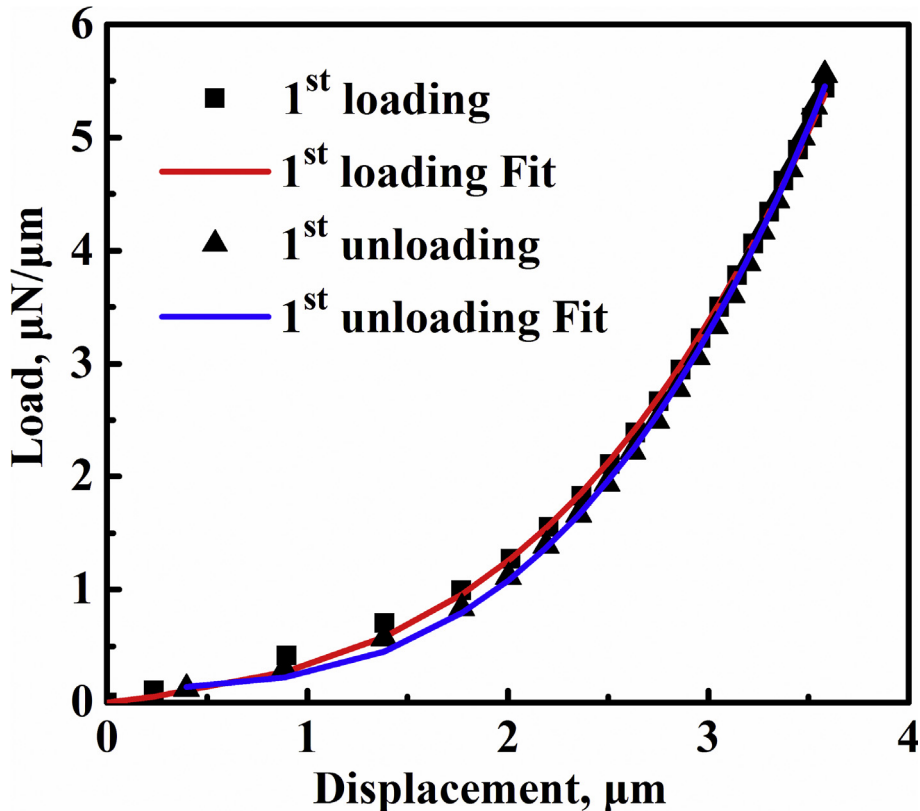


Fig. 6. Repeated load-displacement curves of the microbridge with the corresponding model fitting. (A colour version of this figure can be viewed online.)

value of 99% probability integral with *t*-distribution and *n* denotes the number of data points. In the same way, the residual stress caused by samples fabrication was determined to be 1.51–61.06 MPa.

Based on the above method, the variations of effective Young's modulus fitted by the microbridge theory were obtained. As seen in Fig. 8, variations of the effective Young's modulus in each subsequent cycle have three major aspects. First, the modulus of elasticity fitted using the first loading data is much smaller than each subsequent loading. Most plausible explanation of this result is straightening of the wrinkles in the GO films, which were flattened during the first loading. This flattening affects the measured Young's modulus during the first loading cycle. Shen's study proved using molecular dynamics simulations that the Young's modulus of GO with wrinkles (due to the edge-to-edge interactions between the adjacent individual GO sheets) is lower than the pristine value [12]. Second, the effective Young's modulus obtained from the loading process is apparently different from the modulus obtained from the unloading process fitted by our model. The difference of the loading and the unloading moduli is derived from the energy dissipation between the two processes, which is embodied in the observed displacement hysteresis. Based on the Liu's discussion [32], short crosslinks, such as hydrogen bonds and van der Waals interactions, cause mechanical properties hysteresis between loading and unloading cycles by continuously breaking and reconstructing to dissipate mechanical energy during tensile deformation. Finally, the single factor analysis model (SFAM) [33] was applied to find out the correlation between the loading sequence and the effective Young's modulus *Y*. The Young's modulus of the first loading was not considered due to the self-reinforcing effect. The rejection region, *F*, was determined as

$$F = \frac{S_A/f_A}{S_e/f_e} \quad (11)$$

where *S_A* and *S_e* are the sums of the squares of the standard deviations of the factor *A* and the error *e*, respectively. The variables *f_A* and *f_e* are the number of degrees of freedom of the factor *A* and the error *e*, respectively. The declination square sum, the total declination square sum and the error square sum for the effective Young's modulus of the loading sequence is determined by *S_A = ∑_{i=1}⁵ ∑_{j=1}²² (Y_{i,j} - Ȳ)²*, *S_T = ∑_{i=1}⁵ ∑_{j=1}²² (Y_{i,j} - Ȳ)²* and *S_e = S_T - S_A*, respectively. Thus, *F* = 0.018, and *F_{0.05}(4, 105)* = 5.66 (95%) and *F_{0.01}(4, 105)* = 13.46 (99%). Because *F* is less than *F_{0.05}*, the factor *A*, i.e., the loading sequence (besides the first loading process), has no impact on *Y*. However, if compared with the average Young's modulus, each subsequent cycle displayed an increase. When the first loading process was taken into consideration, the average Young's modulus increased from 71.5 to 91.6 GPa with a total increase of about 28% after three cycles. When the first loading process was not taken into consideration, the average Young's modulus increased from 89.6 to 91.6 GPa with a total increase of about 2.2% after three cycles. Thus, the self-reinforcement property of first loading, which is due to the curved inside structure of the GO sheets, plays an important role in cyclic loading deformation of the GO membrane. The GO membranes were assembled from individual GO sheets, which are unavoidably corrugated due to the irregular distribution of oxygen-rich groups on the surface and thermal fluctuation [34]. The wrinkles make GO sheets incompletely aligned along the same direction [35]. According to Dai's research [30], when the GO membrane is subjected to unidirectional tension, alignment of the graphene sheet along the loading direction improved. Similar behavior has been also found in carbon

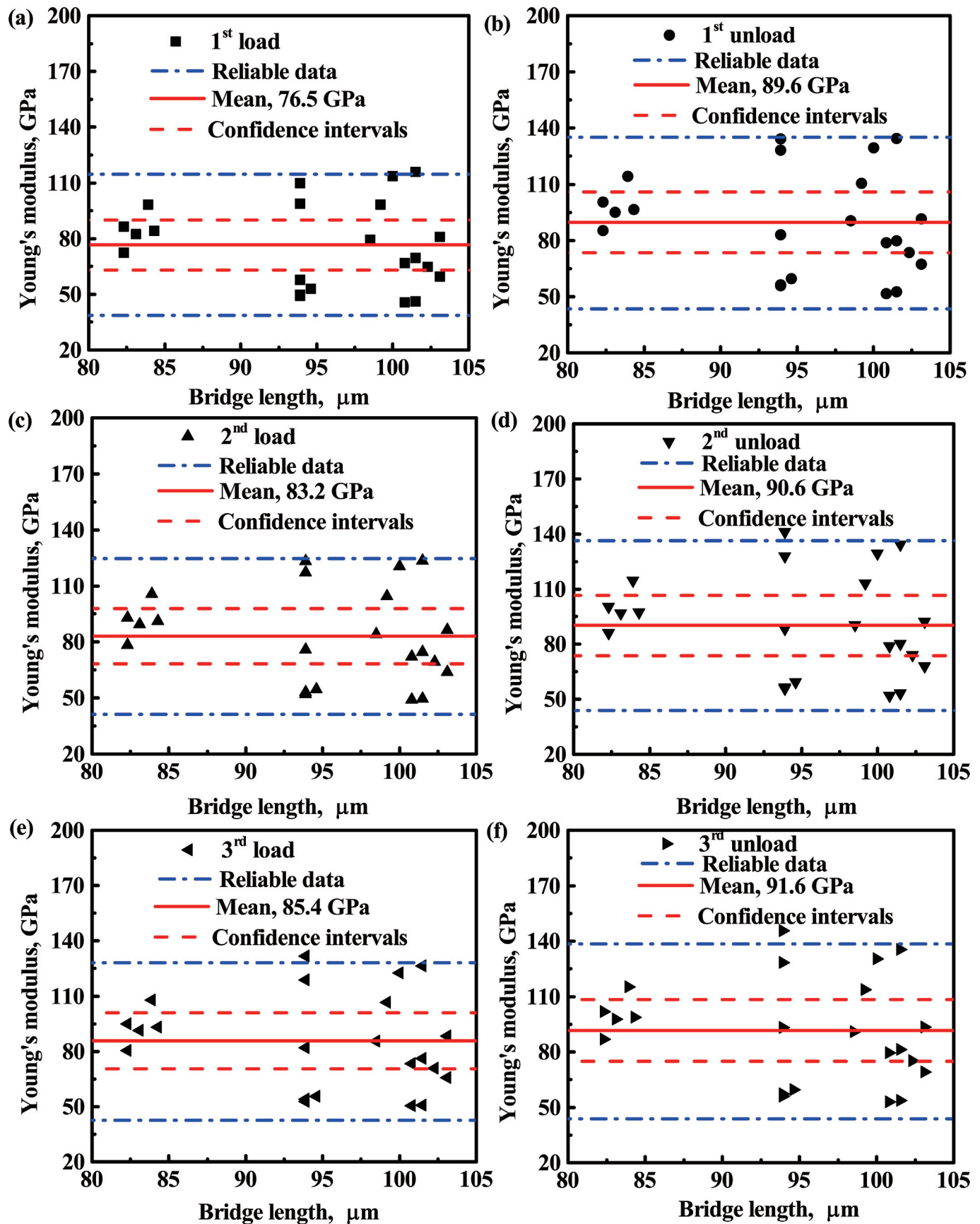


Fig. 7. Effective Young's modulus obtained from: (a) the first loading, (b) the first unloading, (c) the second loading, (d) the second unloading, (e) the third loading and (f) the third unloading versus the microbridge length. (A colour version of this figure can be viewed online.)

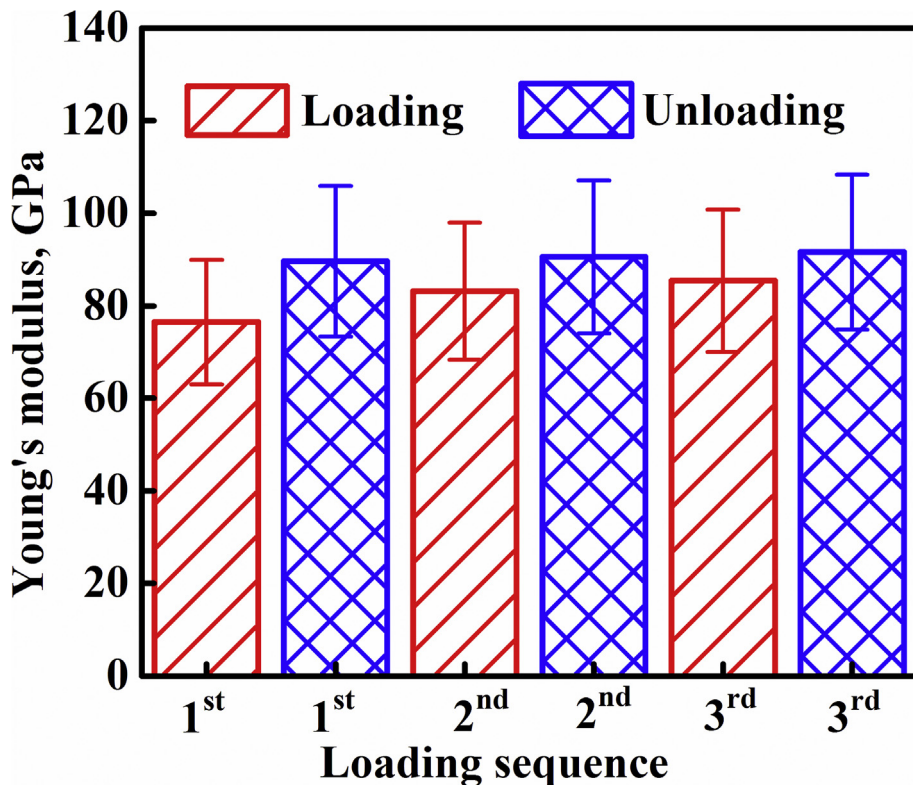


Fig. 8. Loading sequence versus effective Young's modulus fitted by the flexible membrane deformation theory. (A colour version of this figure can be viewed online.)

nanotubes and graphene-based nanocomposites [36,37]. In this case, extra length caused by the alignment of graphene sheets leads to larger strain during the first loading. Due to the rupture and reconstruction of hydrogen bonds and van der Waals interactions, the deformation of the first unloading process is irreversible [32]. Thus, Young's modulus of the first loading is much lower than the value of the subsequent loading cycles. This behavior can be reflected in the difference of load-displacement curves between the first loading and the subsequent loading-unloading. Zhang [38] found that the difference between the first loading curves and the subsequent loading-unloading curves increased as the applied strain increased in cyclic loading-unloading testing. Subsequent loading-unloading curves had little change, which lead to only a small change of the Young's modulus.

Combining the membrane bridge and the deformable tension-shear models, a multiscale model is proposed, where the load-deflection relationship can be rewritten as

$$Q = \frac{8t}{L^3} \left[\frac{Eh}{2(h_0 + h)} \frac{1}{\frac{1}{2} + \frac{1+\cosh(l/l_0)}{\sinh(l/l_0)} (l/l_0)} \right] w_c + \frac{4t\sigma_r}{L} w_c \quad (12)$$

Some parameters of the single layer graphene oxide derived from previous experimental results are listed in Table 1. Given the interlayer spacing of 0.8 nm, 1 nm thickness of the monolayer, 207.6 GPa Young's modulus of the monolayer and 300 nm length of the monolayer, the shear modulus of interlayer galleries within graphene oxide membrane is determined by fitting the force-displacement curve using Eq. (12), which is in the 6.3–19.9 MPa range. The results are in good agreement with the test results obtained by the oscillatory barrier measurements [39].

By using the nanoindenter equipped with a temperature control stage, cyclic loading tests at different temperatures were conducted to study the change of the effective Young's modulus. Five GO microbridge samples were measured at four different temperatures (60, 100, 140 and 180 °C). Before each test, all the bridges stayed at corresponding temperature for 30 min to achieve a relatively steady state. Young's moduli at different temperature can be obtained by fitting the load-displacement curves with flexible membrane deformation theory, which were shown in Fig. 9. The single factor analysis model (SFAM) [33] was applied to find out the correlation between the temperature and the effective Young's modulus in each loading sequence. As seen in Fig. 10, the impact

Table 1
Interlayer spacing of the GO membrane, thickness, Young's modulus, shear modulus and length of the monolayer.

Method	Interlayer spacing h_0 (nm)	Thickness h (nm)	Young's modulus E (GPa)	Length l (nm)	Shear modulus G (MPa)
XRD [3]	0.83				
XRD [40]	0.6–1.1				
AFM [11]		1.1–1.2			
AFM [15]		0.8–1.1			
AFM [41]		0.7	207.6 ± 23.4		
AFM [42]		1	250 ± 150		
SEM AFM [43]				100 nm to a μm	14–35
oscillatory barrier measurements [39]					

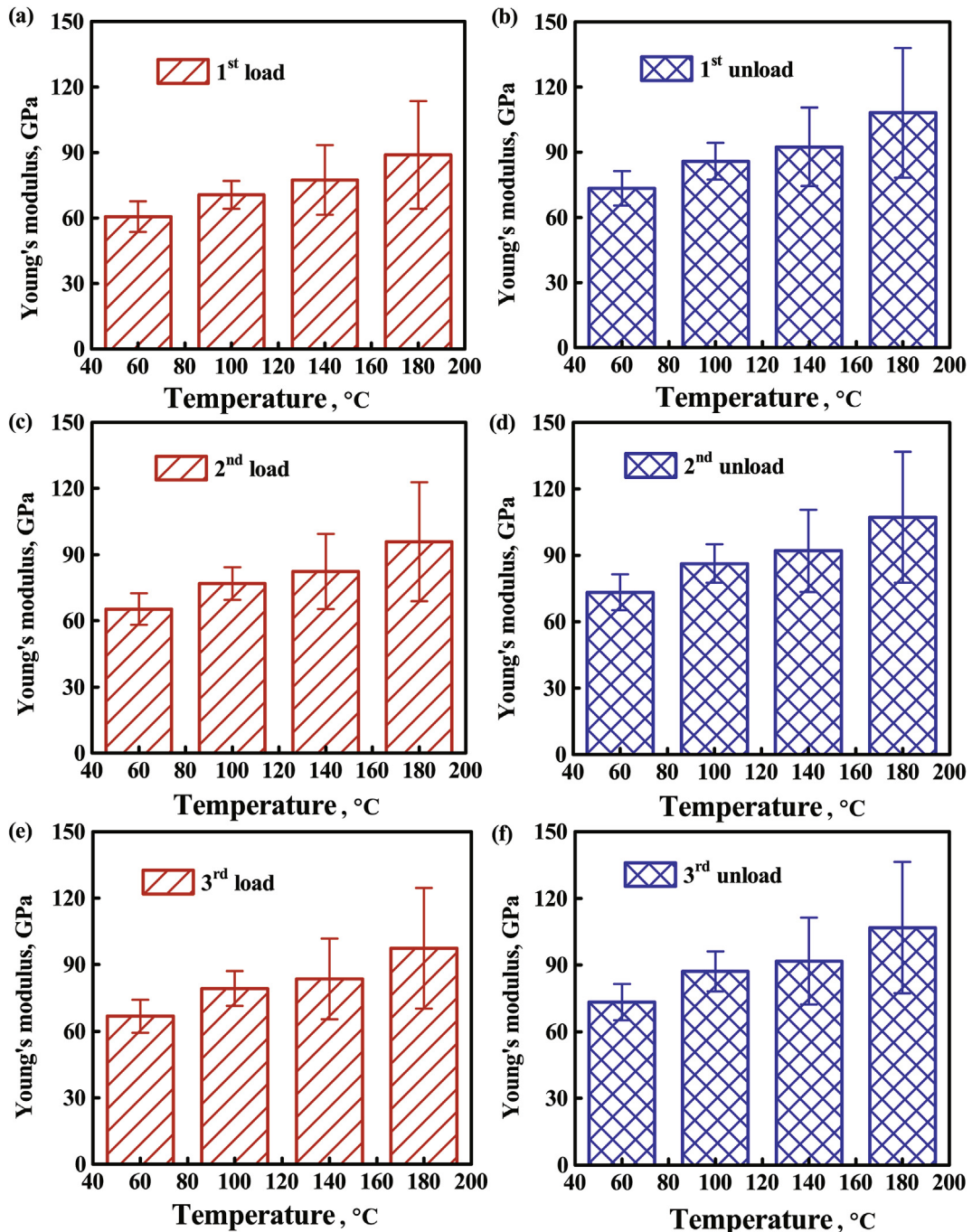


Fig. 9. Temperature versus effective Young's modulus fitted by flexible membrane deformation theory in (a) the first loading, (b) the first unloading, (c) the second loading, (d) the second unloading, (e) the third loading and (f) the third unloading (red: load, blue: unload). (A colour version of this figure can be viewed online.)

degree of temperature on the effective Young's modulus in different loading sequence has three levels, including significant impact (1st load), having an impact (1st unload, 2nd load and 2nd unload) and no impact (3rd load and 3rd unload). According to the thermogravimetric analysis [18], the mass loss of the GO membranes under ambient atmosphere below 200 °C is mainly from the adsorbed water. Interlamellar water molecules weaken the interlayer adhesion and facilitate slippages of nanosheets under external loading by breaking and reforming new hydrogen bonds [17], which results in lower modulus of the GO paper with higher water content [11]. Considering the curved structure of undeformed GO

sheets inside, the membranes were straightened during the first loading, which lead to more broken and reformed hydrogen bonds. Thus, the effective Young's modulus in first loading process was significantly affected by the temperature change. As the number of loading cycles increased, alignment of the GO sheets improved and gradually stabilized, which lead to breaking and reforming hydrogen bonds to become stable. Hence, the impact degree of temperature (below 200 °C) on the effective Young's modulus decreases with the number of loading cycles.

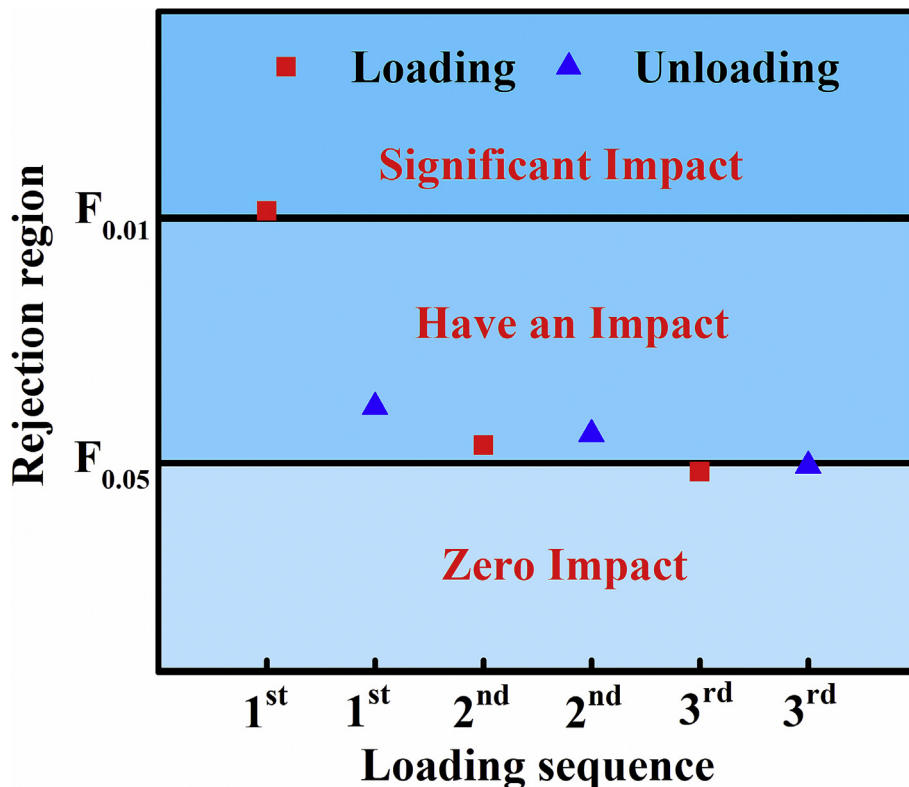


Fig. 10. The impact degree of temperature on the effective Young's modulus in different loading sequence. (A colour version of this figure can be viewed online.)

5. Conclusions

In summary, the microbridge tests are performed to investigate the mechanical properties of the GO membrane. The self-stiffening behavior is investigated by XRD and Raman spectra, which is attributed to straightening and reorientation of graphene sheets. A coupled model is developed based on the membrane bridge model and deformable tension-shear model in view of the deformation characteristics of the GO membrane. In this case, the shear modulus of the graphene oxide membrane can be determined directly from the force-displacement curve. As the number of loading cycles increases, the impact degree of temperature (below 200 °C) on the effective Young's modulus decreases, offering a rational design strategy for devices based on the GO membranes.

Acknowledgments

This study was supported by the National Basic Research Program of China (Grant No. 2012CB937502).

References

- [1] A. Bagri, C. Mattevi, M. Acik, Y.J. Chabal, M. Chhowalla, V.B. Shenoy, Structural evolution during the reduction of chemically derived graphene oxide, *Nat. Chem.* 2 (7) (2010) 581–587.
- [2] C. Chen, Q.-H. Yang, Y. Yang, W. Lv, Y. Wen, P.-X. Hou, M. Wang, H.-M. Cheng, Self-assembled free-standing graphite oxide membrane, *Adv. Mater.* 21 (29) (2009) 3007–3011.
- [3] D.A. Dikin, S. Stankovich, E.J. Zimney, R.D. Piner, G.H.B. Dommett, G. Evmenenko, S.T. Nguyen, R.S. Ruoff, Preparation and characterization of graphene oxide paper, *Nature* 448 (7152) (2007) 457–460.
- [4] H. Li, Z. Song, X. Zhang, Y. Huang, S. Li, Y. Mao, H.J. Ploehn, Y. Bao, M. Yu, Ultrathin, molecular-sieving graphene oxide membranes for selective hydrogen separation, *Science* 342 (6154) (2013) 95–98.
- [5] Y. Song, K. Qu, C. Zhao, J. Ren, X. Qu, Graphene oxide: intrinsic peroxidase catalytic activity and its application to glucose detection, *Adv. Mater.* 22 (19) (2010) 2206–2210.
- [6] B. Xu, S. Yue, Z. Sui, X. Zhang, S. Hou, G. Cao, Y. Yang, What is the choice for supercapacitors: graphene or graphene oxide? *Energy Environ. Sci.* 4 (8) (2011) 2826.
- [7] H. Bi, K. Yin, X. Xie, J. Ji, S. Wan, L. Sun, M. Terrones, M.S. Dresselhaus, Ultra-high humidity sensitivity of graphene oxide, *Sci. Rep.* 3 (2013).
- [8] S. Park, K.-S. Lee, G. Bozoklu, Graphene oxide papers modified by divalent ions—enhancing mechanical properties via chemical cross-linking, *ACS Nano* 2 (3) (2008) 572–578.
- [9] H. Hu, Z. Zhao, W. Wan, Y. Gogotsi, J. Qiu, Ultralight and highly compressible graphene aerogels, *Adv. Mater.* 25 (15) (2013) 2219–2223.
- [10] O.C. Compton, S.T. Nguyen, Graphene oxide, highly reduced graphene oxide, and graphene: versatile building blocks for carbon-based materials, *Small* 6 (6) (2010) 711–723.
- [11] Y. Gao, L.-Q. Liu, S.-Z. Zu, K. Peng, D. Zhou, B.-H. Han, Z. Zhang, The effect of interlayer adhesion on the mechanical behaviors of macroscopic graphene oxide papers, *ACS Nano* 5 (3) (2011) 2134–2141.
- [12] X. Shen, X. Lin, N. Yousefi, J. Jia, J.-K. Kim, Wrinkling in graphene sheets and graphene oxide papers, *Carbon* 66 (2014) 84–92.
- [13] M. Acik, C. Mattevi, C. Gong, G. Lee, K. Cho, M. Chhowalla, Y.J. Chabal, The role of intercalated water in multilayered graphene oxide, *ACS Nano* 4 (10) (2010) 5861–5868.
- [14] N. Wei, C. Lv, Z. Xu, Wetting of graphene oxide: a molecular dynamics study, *Langmuir* 30 (12) (2014) 3572–3578.
- [15] L. Liu, Y. Gao, Q. Liu, J. Kuang, D. Zhou, S. Ju, B. Han, Z. Zhang, High mechanical performance of layered graphene oxide/poly(vinyl alcohol) nanocomposite films, *Small* 9 (14) (2013) 2466–2472.
- [16] H. Chen, M.B. Müller, K.J. Gilmore, G.G. Wallace, D. Li, Mechanically strong, electrically conductive, and biocompatible graphene paper, *Adv. Mater.* 20 (18) (2008) 3557–3561.
- [17] Y. Su, H. Wei, R. Gao, Z. Yang, J. Zhang, Z. Zhong, Y. Zhang, Exceptional negative thermal expansion and viscoelastic properties of graphene oxide paper, *Carbon* 50 (8) (2012) 2804–2809.
- [18] Z.-L. Wang, D. Xu, Y. Huang, Z. Wu, L.-M. Wang, X.-B. Zhang, Facile, mild and fast thermal-decomposition reduction of graphene oxide in air and its application in high-performance lithium batteries, *Chem. Commun.* 48 (7) (2012) 976.
- [19] T.-Y. Zhang, Y.-J. Su, C.-F. Qian, Microbridge testing of silicon nitride thin films deposited on silicon wafers, *Acta Mater.* 48 (2000) 2843–2857.
- [20] H. Espinosa, B. Prorok, M. Fischer, A methodology for determining mechanical properties of freestanding thin films and MEMS materials, *J. Mech. Phys. Solids* 51 (1) (2003) 47–67.
- [21] E.G. Herbert, W.C. Oliver, M.P. de Boer, G.M. Pharr, Measuring the elastic modulus and residual stress of freestanding thin films using nanoindentation

- techniques, *J. Mater. Res.* 24 (09) (2011) 2974–2985.
- [22] M. Huang, T.A. Pascal, H. Kim, W.A. Goddard, J.R. Greer, Electronic–Mechanical coupling in graphene from in situ nanoindentation experiments and multiscale atomistic simulations, *Nano Lett.* 11 (3) (2011) 1241–1246.
- [23] S.P. Kotha, Y. Li, N. Guzelso, Micromechanical model of nacre tested in tension, *J. Mater. Sci.* 36 (8) (2001) 2001–2007.
- [24] B. Ji, H. Gao, Mechanical properties of nanostructure of biological materials, *J. Mech. Phys. Solids* 52 (9) (2004) 1963–1990.
- [25] Y. Liu, B. Xie, Z. Zhang, Q. Zheng, Z. Xu, Mechanical properties of graphene papers, *J. Mech. Phys. Solids* 60 (4) (2012) 591–605.
- [26] S.P. Timoshenko, S. Woinowsky-Krieger, *Theory of Plates and Shells*, McGraw-Hill, New York, 1959.
- [27] Z. Dai, G. Wang, L. Liu, Y. Hou, Y. Wei, Z. Zhang, Mechanical behavior and properties of hydrogen bonded graphene/polymer nano-interfaces, *Compos. Sci. Technol.* 136 (2016) 1–9.
- [28] G. Wang, Z. Dai, L. Liu, H. Hu, Q. Dai, Z. Zhang, Tuning the interfacial mechanical behaviors of monolayer graphene/PMMA nanocomposites, *ACS Appl. Mater. Interfaces* 8 (34) (2016) 22554–22562, <http://dx.doi.org/10.1021/acsami.6b03069>.
- [29] Z. Dai, Y. Gao, L. Liu, P. Pötschke, J. Yang, Z. Zhang, Creep-resistant behavior of MWCNT-polycarbonate melt spun nanocomposite fibers at elevated temperature, *Polymer* 54 (14) (2013) 3723–3729.
- [30] Z. Dai, Y. Wang, L. Liu, X. Liu, P. Tan, Z. Xu, J. Kuang, Q. Liu, J. Lou, Z. Zhang, Hierarchical graphene-based films with dynamic self-stiffening for biomimetic artificial muscle, *Adv. Funct. Mater.* 26 (38) (2016) 7003–7010.
- [31] Z. Dai, C. Weng, L. Liu, Y. Hou, X. Zhao, J. Kuang, J. Shi, Y. Wei, J. Lou, Z. Zhang, Multifunctional polymer-based graphene foams with buckled structure and negative Poisson's ratio, *Sci. Rep.* 6 (2016).
- [32] Y. Liu, Z. Xu, Multimodal and self-healable interfaces enable strong and tough graphene-derived materials, *J. Mech. Phys. Solids* 70 (0) (2014) 30–41.
- [33] H. Ma, C. Cui, X. Li, Z. Sun, Study of high performance autoclaved shell-aggregate from propylene oxide sludge, *Constr. Build. Mater.* 25 (7) (2011) 3030–3037.
- [34] Z. Xu, M.J. Buehler, Geometry controls conformation of graphene sheets: membranes, ribbons, and scrolls, *Acs Nano* 4 (7) (2010) 3869–3876.
- [35] X. Yang, L. Qiu, C. Cheng, Y. Wu, Z.F. Ma, D. Li, Ordered gelation of chemically converted graphene for next-generation electroconductive hydrogel films, *Angew. Chem. Int. Ed.* 50 (32) (2011) 7325–7328.
- [36] Z. Li, R.J. Young, I.A. Kinloch, Interfacial stress transfer in graphene oxide nanocomposites, *ACS Appl. Mat. Interfaces* 5 (2) (2013) 456–463.
- [37] Q. Liang, X. Yao, W. Wang, Y. Liu, C.P. Wong, A three-dimensional vertically aligned functionalized multilayer graphene architecture: an approach for graphene-based thermal interfacial materials, *ACS Nano* 5 (3) (2011) 2392–2401.
- [38] Y. Zhang, S. Gong, Q. Zhang, P. Ming, S. Wan, J. Peng, L. Jiang, Q. Cheng, Graphene-based artificial nacre nanocomposites, *Chem. Soc. Rev.* 45 (9) (2016) 2378–2395.
- [39] K.L. Harrison, L.B. Biedermann, K.R. Zavadil, Mechanical properties of water-assembled graphene oxide langmuir monolayers: guiding controlled transfer, *Langmuir* 31 (36) (2015) 9825–9832.
- [40] N.V. Medhekar, A. Ramasubramaniam, R.S. Ruoff, V.B. Shenoy, Hydrogen bond networks in graphene oxide composite paper: structure and mechanical properties, *ACS Nano* 4 (4) (2010) 2300–2306.
- [41] J.W. Suk, R.D. Piner, J. An, R.S. Ruoff, Mechanical properties of monolayer graphene oxide, *ACS Nano* 4 (11) (2010) 6557–6564.
- [42] C. Gómez-Navarro, M. Burghard, K. Kern, Elastic properties of chemically derived single graphene sheets, *Nano Lett.* 8 (7) (2008) 2045–2049.
- [43] H. Kim, A.A. Abdala, C.W. Macosko, Graphene/polymer nanocomposites, *Macromolecules* 43 (16) (2010) 6515–6530.